Alkaline Earth Titanate (A^ETiO_3) Perovskite Nanoparticles Synthesized from Structurally Characterized Single-Source Alkoxides

Bernadette A. Hernandez-Sanchez, Timothy J. Boyle,* Christina M. Baros, Luke N. Brewer, Thomas J. Headley, Dave R. Tallant, Mark A. Rodriguez, and Bruce A. Tuttle

Sandia National Laboratories, Advanced Materials Laboratory, 1001 University Boulevard Southeast, Albuquerque, New Mexico 87106

Received July 31, 2006. Revised Manuscript Received December 12, 2006

A series of alkaline earth modified titanium *neo*-pentoxide (OCH_2CMe_3, ONep) derivatives were synthesized through the alcoholysis reaction of $[Ti(\mu\text{-ONep})(ONep)_3]_2$ and the respective alkaline earth alkoxide ($A^E(OR)_2$), where $A^E(OR)_2$ = "$Ca(ONep)_2$" (**1**), $Sr_5(\mu_4\text{-O})(\mu_3\text{-ONep})_4(\mu\text{-ONep})_4(HONep)(py)_4$ (**2**), or $[Ba_2(\mu_3\text{-ONep})(\mu\text{-ONep})_2(ONep)(HONep)_3(py)]_2$ (**3**), in pyridine (py) in a 1:1 cation stoichiometry. For each A^E cation, the following mixed-cation species were identified by single-crystal X-ray diffraction as $(py)_2A^E[Ti(\mu\text{-ONep})_2(ONep)_3]_2$, where A^E = Ca (**1a**), Sr (**2a**), and Ba (**3a**). For each species, two square bipyramidal titanium moieties bridge to the single octahedrally bound A^E metal center through four μ-ONep ligands. Two terminal py ligands on the A^E and three terminal ONep ligands on Ti complete their coordination. Compounds **1a**−**3a** were used to synthesize nanoparticles of A^ETiO_3 using solution precipitation (methyl-imidazole:water) and solvothermal (benzyl alcohol) routes. For comparison, we processed stoichiometeric mixtures of the individual precursors under identical conditions as noted for **1**−**3**. The nanoparticles (5−50 nm) synthesized varied in phase from carbonates to perovskites depending on the cation and the synthetic conditions used. On the basis of the comparison of routes, stoichiometric mixtures were better in generating single-phase A^ETiO_3 from the MeIm/H_2O route after calcination, whereas, through solovothermal synthesis routes, single-source and stoichiometric mixtures both gave favorable crystalline results for Sr and Ba.

Introduction

Electroceramic titanate materials have been intensely studied since the early 1940s because they are easily synthesized, chemically and mechanically robust, and exhibit a ferroelectric-to-paraelectric phase transition at or above room temperature. Of these ceramics, barium titanate ($BaTiO_3$ (BT)) is the most widely studied because of its dielectric constant, which varies with particle size and can be fine-tuned (i.e., tunable dielectric) through doping with other alkaline earth titanates (A^ETiO_3) such as strontium titanate ($SrTiO_3$ (ST))[1,2] or calcium titanate ($CaTiO_3$ (CT)).[3] Current research efforts have focused on discovering the novel properties expected for nanoelectroceramics because of the surface-dominated properties in this size regime.[4,5] Because the properties of the pervoskites, such as the Curie temperature (T_c), are critically dependent on the particle size, simple high-yield routes to these nanomaterials are necessary to fully understand these property changes.

Solution routes to nanoelectroceramics are of interest because they are inexpensive and flexible, require a simple experimental setup, and can be easily modified for large-scale reactions. Many solution routes to A^ETiO_3 nanomaterials have employed metal alkoxides ($M(OR)_x$) as part of their process, including: (i) titanium alkoxides ($Ti(OBu^t)_4$), when mixed with A^E-hydroxide precursors, yielded 50 nm BST[6] or (ii) $Ti(OPr^i)_4$, when reacted with A^E-carbonates, produced 55 nm BST powder.[7] In addition, several in situ generated double alkoxides have been successfully used for the synthesis of A^ETiO_3 nanomaterials, such as 10 nm $BaTiO_3$ particles from "$BaTi(OCH_2C_6H_5)_6$"[8] and $BaTiO_3$ rods from "$A^ETi[OCH(CH_3)_2]_6$" (A^E = Ba, Sr).[9] In contrast to these "uncharacterized" intermediates, crystallographically identified species have also been shown to be useful for A^ETiO_3 nanomaterials, including the hydroxy alkoxide $[BaTi(OH)(OPr^i)_5(Pr^iOH)_3]_2$, which formed 30−80 nm $BaTiO_3$

* To whom correspondence should be addressed. Phone: (505) 272-7625. Fax: (505) 272-7336. E-mail: tjboyle@sandia.gov.

(1) Boyle, T. J.; Clem, P. G.; Rodriquez, M. A.; Tuttle, B. A.; Heagy, M. D. *J. Sol−Gel Sci. Technol.* **1999**, *16*, 47−55.
(2) Tagantaev, A. K.; Sherman, V. O.; Astafiev, K. F.; Venkatesh, J.; Setter, N. *J. Electroceram.* **2003**, *11*, 5−66.
(3) Wang, X.; Yamada, H.; Xu, C.-N. *Appl. Phys. Lett.* **2005**, *86*, 022905−3.
(4) Akdogan, E. K. L., M. R.; Safari, A In *Handbook of Low and High Dielectric Constant Materials*; Nawala, H. S., Ed.; Academic Press: San Diego, CA, 1999.
(5) Hernandez-Sanchez, B. A.; Chang, K.-S.; Scancella, M. T.; Burris, J. L.; Kohli, S.; Fisher, E. R.; Dorhout, P. K. *Chem. Mater.* **2005**, *17*, 5909−5919.
(6) Qi, J. Q.; Wang, Y.; Chen, W. P.; Li, L. T.; Chan, H. L. W. *J. Solid State Chem.* **2005**, *178*, 279−284.
(7) Arya, P. R.; Jha, P.; Ganguli, A. K. *J. Mater. Chem.* **2003**, *13*, 415−423.
(8) Niederberger, M.; Garnweitner, G.; Pinna, N.; Antonietti, M. *J. Am. Chem. Soc.* **2004**, *126*, 9120−9126.
(9) Urban, J. J.; Yun, W. S.; Gu, Q.; Park, H. *J. Am. Chem. Soc.* **2002**, *124*, 1186−1187.

10.1021/cm061798+ CCC: $37.00
Published on Web 02/14/2007

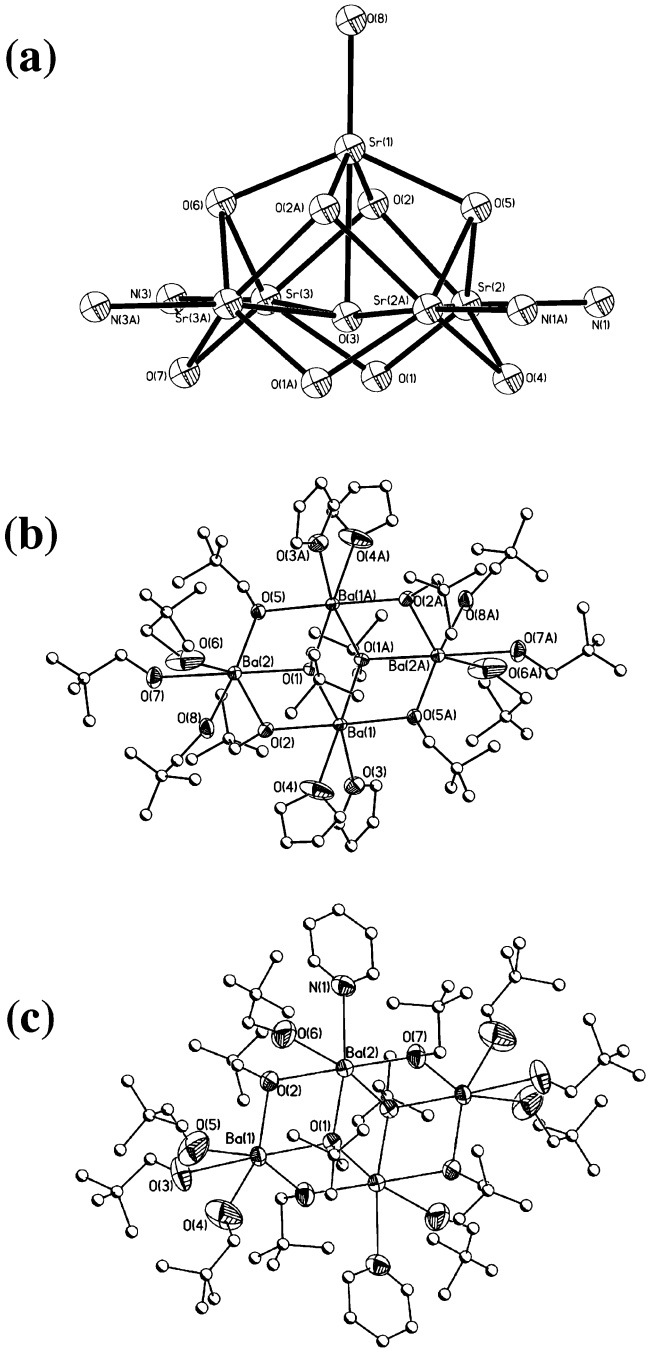

Figure 1. Structure plots of (a) **2**, (b) **A**, and (c) **3**. Thermal ellipsoids of the heavier atoms are drawn at the 30% level. Carbon atoms are shown as simple spheres and hydrogen atoms are omitted for clarity.

particles[10] or the commercially available, but crystallographically uncharacterized double alkoxide, $BaTi(O_2CC_7H_{15})[OC(CH_3)_2]_5$, which produced 12 nm $BaTiO_3$ particles.[11]

The widespread use of $M(OR)_x$ in the production of ceramic materials is not an accident, because these compounds are often commercially available and possess high solubility, high volatility, and low decomposition temperatures, all of which are necessary for nanoparticle production. Further, these properties can be easily tailored through ligand manipulation. However, the use of A^E precursors such as hydroxides, acetates, and carbonates to produce A^ETiO_3 ceramics indicate the limited number of acceptable A^E alkoxide ($A^E(OR)_2$) precursors that are available. The A^E precursors (i.e., OH, CO_3, and O_2CMe) have limited solubility, and the variable intermediate compounds produced between the reaction of $M(OR)_x$ and A^E create nonuniformities in the final bulk ceramics. Therefore, developing $A^ETi(OR)_6$ and $A^E(OR)_2$ compounds is of interest for the synthesis of homogeneous high-quality nanoceramics.

Previously, we have shown that the structure of the $M(OR)_x$ is critical in determining the properties of simple nanoceramic morphology and phase, thus we were interested in learning if the $A^E(OR)_6$ structure would affect the synthesis of complex ceramics.[12−14] Of the precursors described in the literature that could be used to synthesize A^ETiO_3 nanoparticles,[6−11] the few that have been characterized by single-crystal X-ray diffraction possess large Ti:A^E ratios which does not bode well for the formation of A^ETiO_3 nanomaterials.[15−24] Therefore, we undertook new synthetic strategies to control the A^ETiO_3 nanoparticle composition, crystallinity, morphology, and size through carefully constructed $M(OR)_x$. To realize this control, it is helpful to have one systematic variation in the family of compounds investigated.

The utility of single-source precursors has been studied extensively for sol−gel processing, but not as rigorously for nanoparticle synthesis. This is most likely a reflection of the lack of acceptable precursors for the systems of interest. From complex mixtures, we have identified a new family of mixed-cation $A^ETi(OR)_6$ *neo*-pentoxide (ONep = OCH_2CMe_3) precursors through the reaction of titanium *neo*-pentoxide ($[Ti(\mu\text{-ONep})(ONep)_3]_2$)[25] and the respective $A^E(ONep)_2$ derivative: "$Ca(ONep)_2$" (**1**); $Sr_5(\mu_4\text{-O})(\mu_3\text{-ONep})_4(\mu\text{-ONep})_4(HONep)(py)_4$ (**2**);[1,26] and $[Ba_2(\mu_3\text{-ONep})(\mu\text{-ONep})_2(ONep)(HONep)_3(py)]_2$ (**3**)[1] in pyridine (py) in a 1:1 cation stoichiometry. For each A^E cation, the following species

(10) Veith, M.; Mathur, S.; Lecerf, N.; Huch, V.; Decker, T. *J. Sol−Gel Sci. Technol.* **2000**, *15*, 145−158.
(11) O'Brien, S.; Brus, L.; Murray, C. B. *J. Am. Chem. Soc.* **2001**, *123*, 12085−12086.
(12) Boyle, T. J.; Hernandez-Sanchez, B. A.; Baros, C. M.; Brewer, L. N.; Rodriguez, M. A. *Chem. Mater.* **2006**, submitted.
(13) Boyle, T. J.; Bunge, S. D.; Andrews, N. L.; Matzen, L. E.; Sieg, K.; Rodriquez, M. A.; Headly, T. J. *Chem. Mater.* **2004**, *16*, 3279−3288.
(14) Boyle, T. J.; Bunge, S. D.; Clem, P. G.; Richardson, J.; Dawley, J. T.; Ottley, L. A. M.; Rodriguez, M. A.; Tuttle, B. A.; Avilucea, G.; Tissot, R. G. *Inorg. Chem.* **2005**, *44*, 1309−1318.
(15) Starikova, Z. A.; Yanovsky, A. I.; Kotova, N. M.; Yanovskaya, M. I.; Turova, N. Y.; Benilan, D. *Polyhedron* **1997**, *16*, 4347−4351.
(16) Turevskaya, E. P.; Kessler, V. G.; Turova, N. Y.; Pisarevsky, A. P.; Yanovsky, A. I.; Struchkov, Y. T. *Chem. Commun.* **1994**, 2303−2304.
(17) Yanovsky, A. I.; Yanovskaya, M. I.; Limar, V. K.; Kessler, V. G.; Turova, N. Y.; Struchkov, Y. T. *Chem. Commun.* **1991**, *22*, 1605−1606.
(18) Yanovsky, A. I.; Turevskaya, E. P.; Yanovskaya, M. I.; Kessler, V. G.; Turova, N. Y.; Pisarevskii, A. P.; Struchkov, Y. T. *Zh. Neorg. Khim. (Russ.)* **1995**, *40*, 355.
(19) Yanovsky, A. I.; Starikova, Z. A.; Yanovskaya, M. I.; Kotova, N. M.; Turova, N. Y. *Zh. Neorg. Khim. (Russ.)* **2003**, *48*, 1456.
(20) Baxter, I.; Drake, S. R.; Hursthouse, M. B.; Malik, K. M. A.; Mingos, D. M. P.; Plakatouras, J. C.; Otway, D. J. *Polyhedron* **1998**, *17*, 625−639.
(21) Veith, M.; Mathur, S.; Huch, V. *Inorg. Chem.* **1997**, *36*, 2391−2399.
(22) Malpezzi, L.; Zucchini, U.; Dall'Occo, T. *Inorg. Chim. Acta* **1991**, *180*, 245−249.
(23) Gaskins, B.; Lannutti, J. J.; Finnen, D. C.; Pinkerton, A. A. *Acta Crystallogr., Sect. C* **1994**, *50*, 1387−1390.
(24) Day, V. W.; Eberspacher, T. A.; Klemperer, W. G.; Liang, S. *Chem. Mater.* **1995**, *7*, 1607−1608.
(25) Boyle, T. J.; Alam, T. M.; Mechenbier, E. R. *Inorg. Chem.* **1997**, *36*, 3293−3300.
(26) Boyle, T. J.; Tafoya, C. J.; Scott, B. L.; Ziller, J. W. *J. Coord. Chem.* **2000**, *51*, 361−378.

Table 1. Data Collection Parameters for A, 3, and 1a−3a

	A	3
chem. formula	$Ba_4O_{16}C_{76}H_{168}$	$Ba_4N_2O_{14}C_{80}H_{164}$
FW	1887.46	1927.52
T (K)	153(2)	297(2)
space group	triclinic, $P\bar{1}$	triclinic, $P\bar{1}$
a (Å)	12.774(2)	13.122(3)
b (Å)	14.315(3)	14.390(4)
c (Å	15.859(3)	16.184(4)
α (deg)	84.922(3)	77.964(5)
β (deg)	66.788(3)	66.517(4)
γ (deg)	66.947(3)	68.559(4)
V (Å^3)	2444.9(7)	2601.9(1)
Z	1	1
D_{calcd} (mg/m^3)	1.282	1.229
λ (Mo, Kα) (mm $^{-1}$))	1.640	1.542
R1[a] (%) (all data)	5.63 (10.91)	7.84 (12.43)
wR2[b] (%) (all data)	13.44 (16.84)	22.03 (25.73)

	1a	2a	3a
chem. formula	$CaTi_2O_{10}N_2C_{60}H_{120}$	$SrTi_2O_{10}N_2C_{60}H_{120}$	$BaTi_2O_{10}N_2C_{60}H_{120}$
FW	1165.46	1213.00	1262.72
T (K)	203(2)	203(2)	203(2)
space group	monoclinic, $C2/c$	monoclinic, $C2/c$	monoclinic, $P2(1)/c$
a (Å)	26.306(3)	26.829(4)	27.721(3)
b (Å)	13.600(2)	13.859(2)	13.601(1)
c (Å)	20.366(3)	20.427(3)	20.5859(2)
β (deg)	109.969(3)	109.515(3)	111.698(2)
V (Å^3)	6848.5(2)	7159(2)	7211.4(1)
Z	4	4	4
D_{calcd} (mg/m^3)	1.130	1.125	1.163
λ (Mo, Kα) (mm $^{-1}$))	0.359	1.009	0.804
R1[a] (%) (all data)	13.48 (27.77)	5.85 (8.61)	8.18 (13.85)
wR2[b] (%) (all data)	35.05 (42.95)	15.09 (16.76)	19.36 (22.86)

[a] $R1 = \sum||F_o| - |F_c||/\sum; |F_o| \times 100$. [b] $wR2 = [\sum w(F_o^2 - F_c^2)^2/\sum(w|F_o|^2)^2]^{1/2} \times 100$.

were identified by single-crystal X-ray diffraction as $(py)_2A^E$-$[Ti(\mu\text{-ONep})_2(ONep)_3]_2$, where A^E = Ca (**1a**), Sr (**2a**), and Ba (**3a**). Compounds **1a**−**3a** possess the simple, single structural variation of Ti−O−A^E coordination for exploration of the controlling factors in A^ETiO_3 nanoparticle synthesis. Therefore, both solution and solvothermal routes were used to generate A^ETiO_3 nanoparticles from **1a**−**3a**, and these results were compared to particles synthesized from stoichiometric mixtures of $[Ti(\mu\text{-ONep})(ONep)_3]_2$) and **1**−**3**. Details of the synthesis and characterization of these precursors and the subsequent materials generated from them are presented.

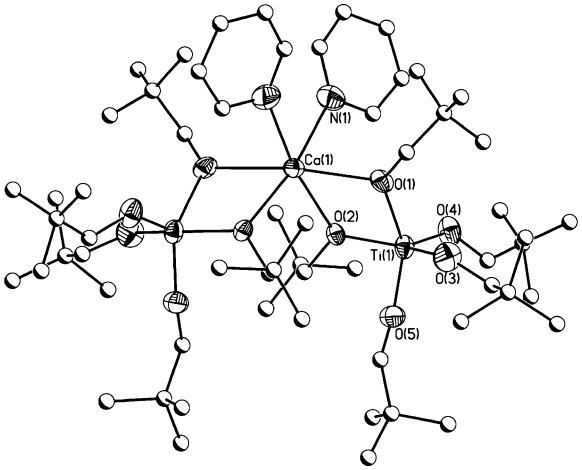

Figure 2. Representative structural plot of **1a**−**3a** (compound **1a** shown). Thermal ellipsoids of the heavier atoms are drawn at the 30% level. Carbon atoms are shown as simple spheres and hydrogen atoms are omitted for clarity.

Experimental Section

All compounds described below were handled with rigorous exclusion of air and water using standard Schlenk line and glovebox techniques. The following chemicals were used as received and were stored under argon (Aldrich): H-ONep, Sr°, Ba°, CaI_2, KNR_2 where R = $Si(CH_3)_3$, benzyl alcohol (BzOH), pyridine (py), and toluene (tol). Solvents were stored in SureSeal bottles. The following compounds were synthesized according to published procedures: $Ca[N(SiMe_3)_2]_2$,[27] $[Ti(\mu\text{-ONep})(ONep)_3]_2$,[25] **2**,[26] and **3**.[1] Although the synthesis of **3** was previously discussed,[1] the structural aspects were not fully described. Thus, the synthesis of **3** is provided below and begins with the synthesis of $[Ba_2(\mu_3\text{-ONep})(\mu\text{-ONep})_2(ONep)(HONep)_3(THF)_2]_2$ (**A**), which is the precursor for **3**.

FT−IR data were obtained on a Bruker Vector 22 MIR Spectrometer using KBr pellets under an atmosphere of flowing nitrogen. Elemental analyses were performed on a Perkin-Elmer 2400 CHN-S/O elemental analyzer. High resolution ^{1}H and ^{13}C NMR spectra were obtained at 399.8 and 100.6 MHz, respectively, on crystalline samples redissolved in deuterated pyridine (py-d_5), in a Bruker DRX400 instrument using a 5 mm broad-band probe. Standard pulse sequences were used in all cases and all spectra were referenced to the deuterated solvent signal.

$[Ba_2(\mu_3\text{-ONep})(\mu\text{-ONep})_2(ONep)(HONep)_3(THF)_2]_2$ (A). To a Schlenk flask containing Ba° (7.82 g, 56.9 mmol) in THF (100 mL) H-ONep (20.1 g, 228 mmol) was added, and the reaction mixture was heated at reflux temperatures for 48 h until the metal was consumed completely. The solution was cooled to room temperature, dried in vacuo, and transferred to a glovebox. The structure of the crystals isolated from the mother liquor is shown in Figure 1b. This product was used to synthesize **3**, Figure 1c.

(27) Tanner, P. S.; Burkey, D. J.; Hanusa, T. P. *Polyhedron* **1995**, *14*, 331−333.

Table 2. Experimental Results for ABO_3 Nanoparticles Synthesized from the Solution Precipitation Route (MeIm/H_2O) and Calcined at 650 °C

precursor(s)	targeted ABO_3	TEM size (nm), shape	major phase (minor phase)
1a	$CaTiO_3$	10−50, spherical	mixed
1 + $Ti(ONep)_4$	$CaTiO_3$	50, spherical	orthorhombic (none)
2a	$SrTiO_3$	30−50, spherical	cubic (carbonate)
2 + $Ti(ONep)_4$	$SrTiO_3$	20−50, spherical/rectangular	cubic (none)
3a	$BaTiO_3$	10−50, spherical	tetragonal (carbonate)
3 + $Ti(ONep)_4$	$BaTiO_3$	10−20, spherical	tetragonal (orthotitante)

Table 3. Experimental Results for ABO_3 Nanoparticles Synthesized from the Solvothermal Route (BZOH)

precursor(s)	targeted ABO_3	TEM size (nm), shape	major phase (minor phase)
1a	$CaTiO_3$	30−50, spherical	orthorhombic[a] (carbonate)
1 + $Ti(ONep)_4$	$CaTiO_3$	50, spherical	orthorhombic[a] (carbonate)
2a	$SrTiO_3$	10, spherical	cubic (none)
2 + $Ti(ONep)_4$	$SrTiO_3$	15, spherical	cubic (none)
3a	$BaTiO_3$	50−100, spherical	tetragonal[a] (carbonate)
3 + $Ti(ONep)_4$	$BaTiO_3$	5−10, spherical	tetragonal (none)

[a] Particles calcined at 650 °C.

$[Ba_2(\mu_3\text{-ONep})(\mu\text{-ONep})_2(ONep)(HONep)_3(py)]_2$ (3) was isolated after washing **A** with toluene. The resulting white powder was extracted with py. The volatile portion of the reaction mixture was drastically reduced by rotary evaporation, and X-ray quality crystals were isolated by cooling to −35 °C. Crystalline yield: 11.0 g (41.0%). FT−IR (KBr pellet, cm^{-1}): 2952 (s), 2362 (w), 1477 (w), 1396 (w), 1357 (w), 1261 (w), 1099 (s), 1019 (m), 802 (m), 550 (w). ^1H NMR (400 mHz, py-d_5): δ 3.49 (2.0H, s, $OCH_2C(CH_3)_3$), 1.02 (9.2H, s, $OCH_2C(CH_3)_3$). $^{13}C\{^1H\}$ NMR (100.1 MHz, py-d_5): δ 72.7 ($OCH_2C(CH_3)_3$), 33.1 ($OCH_2C(CH_3)_3$), 26.7-($OCH_2C(CH_3)_3$). Elem. Anal. Calcd for $C_{80}H_{162}Ba_4N_2O_{14}$: C, 49.90; H, 8.49; N, 1.45. Calcd for $C_{70}H_{152}Ba_4O_{14}$ (−2 py): C, 47.57; H, 8.67; N, 0.00. Found: C, 47.06; H, 8.64; N, 0.00.

$(py)_2Ca[Ti(\mu\text{-ONep})_2(ONep)_3]_2$ (1a). $Ca[N(SiMe_3)_2]_2$ (0.455 g, 1.26 mmol) dissolved in py was slowly added to a stirring solution of clear $[Ti(\mu\text{-ONep})(ONep)_3]_2$ (1.00 g, 1.26 mmol) dissolved in pyridine to yield a clear dark orange solution. Upon addition of H-ONep (0.277 g, 3.15 mmol) dissolved in py to form the in situ "$Ca(ONep)_2$", the color of the reaction lightened to clear yellow. After stirring for 12 h, the reaction volume was drastically reduced by rotary evaporation and cooled to −35 °C until X-ray quality crystals were isolated. Yield: 0.667 g (45.3%). FT−IR (KBr pellet, cm^{-1}): 2953 (s), 2866 (m), 2362 (w), 1598 (w), 1479 (m), 1393 (w), 1362 (w), 1065 (s), 1021 (m), 935 (w), 803 (w), 752 (w), 703 (w), 643 (w), 469 (w). ^1H NMR (400 MHz, py-d_5): δ 3.49 (2.0H, s, $OCH_2C(CH_3)_3$), 1.02 (9.4H, s, $OCH_2C(CH_3)_3$). ^{13}CNMR (100.1 MHz, py-d_5): δ 72.5 ($OCH_2C(CH_3)_3$), 33.14 ($OCH_2C(CH_3)_3$), 26.6 ($OCH_2C(CH_3)_3$). Elem. Anal. Calcd for $C_{60}H_{120}CaN_2O_{10}Ti_2$: C, 61.80; H, 10.39; N, 2.40. Found: C, 60.08; H, 10.20; N, 2.26.

$(py)_2Sr[Ti(\mu\text{-ONep})_2(ONep)_3]_2$ (2a). To a solution of **2** (0.390 g, 0.252 mmol) dissolved in ∼10 mL of py, $[Ti(\mu\text{-ONep})(ONep)_3]_2$ (1.00 g, 1.26 mmol) was added, and the solution was allowed to stir, forming a clear light yellow solution. After 12 h, the volatile portion of the reaction mixture was drastically reduced by rotary evaporation, and X-ray quality crystals were isolated by cooling to −35 °C. Yield: 1.32 g (86.2. %). FT−IR (KBr pellet, cm^{-1}): 2965 (s), 1479 (w), 1392 (w), 1062 (s), 1020 (m), 703 (m), 466 (w). ^1H NMR (400 MHz, py-d_5): δ 3.49 (2.0H, s, $OCH_2C(CH_3)_3$), 1.02 (9.0H, s, $OCH_2C(CH_3)_3$). $^{13}C\{^1H\}$ NMR (100.1 MHz, py-d_5): δ 73.9 ($OCH_2C(CH_3)_3$), 34.3 ($OCH_2C(CH_3)_3$), 27.9 ($OCH_2C(CH_3)_3$). Elem. Anal. Calcd for $C_{60}H_{120}N_2O_{10}SrTi2$: C, 59.46; H, 9.99; N, 2.31. Found: C, 58.1; H, 10.05; N, 2.15.

$(py)_2Ba[Ti(\mu\text{-ONep})_2(ONep)_3]_2$ (3a). To a solution of **3** (0.609 g, 0.315 mmol) dissolved in ∼10 mL of py, $[Ti(\mu\text{-ONep})(ONep)_3]_2$ (1.00 g, 1.26 mmol) was added, and the solution was allowed to stir, forming a clear light yellow solution. After 12 h, the volatile portion of the reaction mixture was drastically reduced by rotary evaporation, and X-ray quality crystals were isolated by cooling to −35 °C. Yield: 1.23 g (77.3%). FT−IR (KBr pellet, cm^{-1}): 2955 (s), 1656 (w), 1479 (w), 1363 (m), 1075 (s), 1022 (s), 803 (m), 702 (w), 466 (w). ^1H NMR (400 MHz, py-d_5): δ 3.49 (2.0H, s, $OCH_2C(CH_3)_3$), 1.02 (14.3H, s, $OCH_2C(CH_3)_3$). $^{13}C\{^1H\}$ NMR (100.1 MHz, py-d_5): δ 27.2 ($OCH_2C(CH_3)_3$). Elem. Anal. Calcd for $C_{60}H_{120}N_2O_{10}BaTi_2$: C, 57.06; H, 9.60; N, 2.22. Found: C, 55.45; H, 9.56; N, 1.99.

General X-ray Crystal Structure Information.[28] Each crystal was mounted onto a thin glass fiber from a pool of Fluorolube and immediately placed under a stream of vapor from liquid N_2, on a Bruker AXS diffractometer. The radiation used was graphite-monochromatized Mo Kα radiation (λ = 0.7107 Å). The lattice parameters were optimized from a least-squares calculation on carefully centered reflections. Lattice determination and data collection were carried out using SMART version 5.054 software. Data reduction was performed using SAINT version 6.01 software. The structure refinement was performed using XSHELL 3.0 software. The data were corrected for absorption using the SADABS program within the SAINT software package.

It is of note that crystal structures of metal alkoxides are often plagued by disorder within the atoms of the ligand chain. This phenomenon subsequently leads to larger *R* values. Each structure was solved using direct methods. This procedure yielded the heavy atoms, along with a number of C, O, and N atoms. Subsequent Fourier synthesis yielded the remaining atom positions. Additional information concerning the data collection and final structural solutions (Table 1) of these compounds can be found in the supplemental information or by accessing CIF files through the Cambridge Crystallographic Data Base.

General Synthesis of A^ETiO_3 Nanoparticles. Two general synthetic routes, solution precipitation (a) and solvothermal (b), were explored to synthesize the pervoskite nanoparticles: from (i) the single-source $(py)_2A^ETi_2(ONep)_{10}$ (**1a**−**3a**) and (ii) stoichiometric amounts of individual $M(OR)_x$ (i.e.; $[Ti(\mu\text{-ONep})(ONep)_3]_2$ and **1**, **2**, or **3**).

(a) Solution Precipitation. The first route used a 14.5/0.5 mL ratio of 1-methyl imidazole and water (MeIm/H_2O), which was placed in a two-necked, round-bottom flask equipped with a reflux condenser and a septum. Under flowing argon, the MeIm/H_2O solution was brought to reflux conditions (∼200 °C) and the desired precursor dissolved in py was injected via syringe. A white precipitate formed immediately; the mixture was stirred for 30 min

(28) The listed versions of SAINT, XSHELL, SHELXTL, and SADABS Software used in this analysis were from Bruker Analytical X-Ray Systems Inc., 6300 Enterprise Lane, Madison, WI 53719.

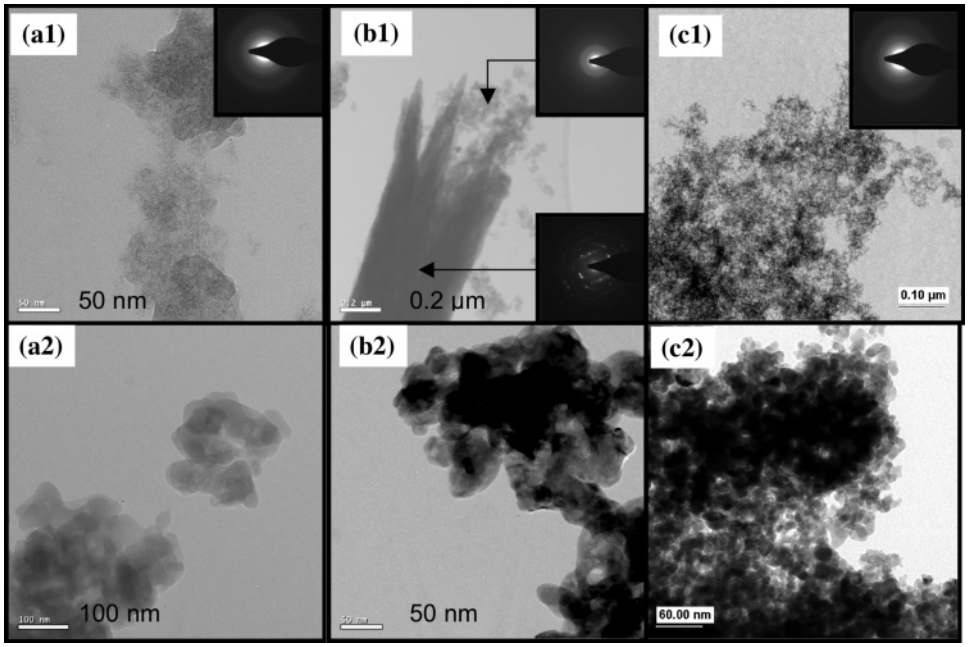

Figure 3. TEM images of nanoceramics generated from the MeIm/H_2O route and the respective single-source precursors: for the as-prepared particles from (a1) **1**, (b1) **2**, and (c1) **3** and images of the calcined (650 °C) nanoceramics from (a2) **1**, (b2) **2**, and (c2) **3**.

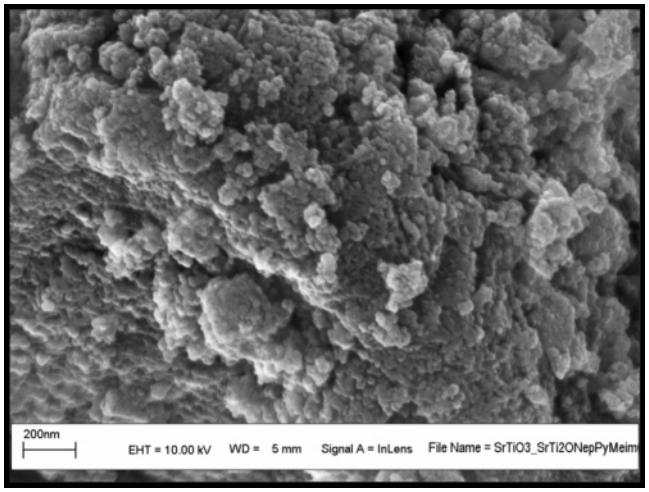

Figure 4. SEM image of **2a** calcined (650 °C) nanoceramic from the MeIm/H_2O route, illustrating the micrometer size distribution and morphology of the particles.

at 197 °C and then allowed to cool to room temperature. The as-prepared particles were collected by centrifugation, rinsed with ethanol, air-dried, and calcined in a tube furnace under flowing argon at 600 °C for 1 h.

(b) Solvothermal. The second route used a 45 mL Parr acid digestion bomb. In the glove box, the desired precursors were dissolved in ~15 mL of benzyl alcohol (BzOH), and the clear solutions were transferred to the Teflon liners and placed in the bomb. The bomb was taken out of the glove box, and the reaction was heated to 200 °C for 48 h. The white precipitate was collected by centrifugation and rinsed with ethanol.

Scanning Electron Microscopy (SEM). The calcined samples were dispersed onto carbon tape and coated with gold palladium using an Edwards sputter coater. Samples were imaged using a Zeiss Supra 55VP field emitter gun scanning electron microscope (FEGSEM). A Noran EDS detector and Noran System Six software were used for the acquisition of EDS spectra.

Transmission Electron Microscopy (TEM). An aliquot of the particles dispersed in ethanol was placed directly onto a carbon type-B copper transmission electron microscopy (TEM) grid (300 mesh) purchased from Ted Pella, Inc. The aliquot was then allowed to dry overnight. The resulting particles were studied using a Philips CM 30 TEM operating at a 300 kV accelerating voltage.

Powder X-ray Diffraction. The nanoparticles were mounted directly onto a zero background substrate (Si (510)) purchased from The Gem Dugout. The average Bravais lattice crystal symmetry and the cell parameters for the nanoscale materials were found using powder X-ray diffraction (PXRD) patterns collected on a PANalytical powder diffractometer with Cu Kα radiation (1.5406 Å) and a RTMS X'Celerator detector. Patterns were analyzed with the JADE software program.[29] The average crystallite sizes for the materials were determined from the full width at half-maximum (fwhm) of the (101) reflection for the cubic phase of A^ETiO_3 using the single-line parameterized Scherrer equation. Instrument broadening was corrected using a NIST standard, LaB_6.

Results and Discussion

As mentioned, $M(OR)_x$ are ideal precursors for the formation of nanocrystalline complex ceramic materials, and a search of the literature reveals very few $A^E(OR)_2$ species available for the synthesis of A^ETiO_3 materials. For example, three Ca alkylalkoxide derivatives have been reported: the methoxy ethoxy,[30] 3,3-*iso*-propoxymethyl-2,2-dimethylpropoxy,[31] and ethoxy[32,33] derivatives. Several arylalkoxide species have also been crystallographically characterized,[34−38] and we recently reported on another family of $Ca(OAr)_2(THF)_x$ derivatives[12] that substantially increases the number

(29) *Jade XRD Pattern Processing*; MDI, Inc.: Livermore, CA, 1999.
(30) Goel, S. C.; Matchett, M. A.; Chiang, M. Y.; Buhro, W. E. *J. Am. Chem. Soc.* **1991**, *113*, 1844−5.
(31) Herrmann, W. A.; Huber, N. W.; Priermeier, T. *Angew. Chem., Int. Ed.* **1994**, *33*, 105−107.
(32) Turova, N. Y.; Turevskaya, E. P.; Kessler, V. G.; Yanovsky, A. I. *Chem. Commun.* **1993**, 21−23.
(33) Yanovsky, A. I.; Turova, N. Y.; Turevskaya, E. P.; Kessler, V. G. *Zh. Neorg. Khim. (Russ.)* **1993**, *38*, 779.
(34) Deacon, G. B.; Forsyth, C. M.; Junk, P. C. *J. Organomet. Chem.* **2000**, *607*, 112−119.

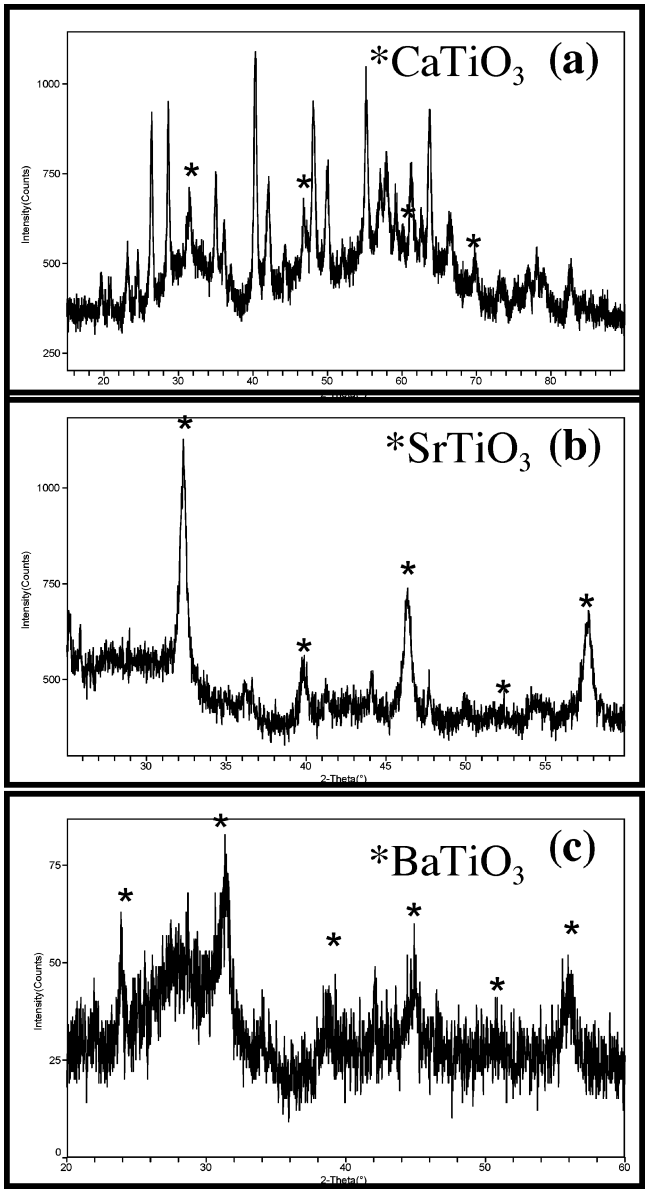

Figure 5. XRD patterns of calcined (650 °C) nanoceramics from the MeIm/H_2O route and the respective single-source precursor: (a) **1a** made CaO, TiO_2 and $CaTiO_3$; (b) **2a** made $SrTiO_3$ and $SrCO_3$, whereas (c) **3a** made $BaTiO_3$ and $BaCO_3$.

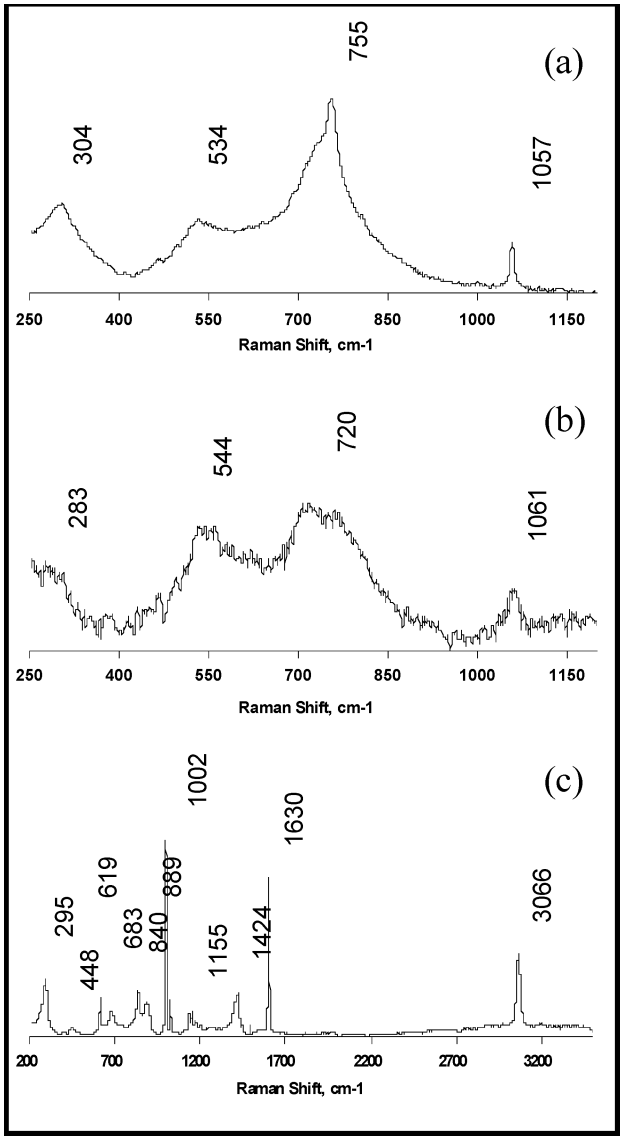

Figure 6. Raman spectra of the $BaTiO_3$ nanoparticles isolated from solution precipitation and solvothermal routes: (a) **1a**, MeIm/H_2O; (b) **1** + [Ti(μ-ONep)(ONep)$_3$]$_2$, MeIm/H_2O; and (c) **1** + [Ti(μ-ONep)(ONep)$_3$]$_2$, BzOH.

of available precursors. Literature reports for "$Sr(OR)_2$" compounds include [$Sr_2(\mu_3$-OPh)(μ-OPh)$_2$(OPh)(THF)$_2$]$_2$[39], $Sr(TBP)_2(THF)_3$ (TBP = $OC_6H_2(CMe_3)_3$-2,4,6),[40] and (OPP)-$Sr(\mu$-OPP)$_3$Ba (OPP = $OC_6H_3(C_6H_5)_2$-2,6).[34] Two additional compounds, $Sr_5(\mu_4$-O)(μ_3-ONep)$_4$(μ-ONep)$_4$(HONep)(solv)$_4$ (solv = THF, py (**2**)),[26] complete this list. In this same report for **2**, we also discussed the ONep derivative of Ba, which formed [$Ba_2(\mu_3$-ONep)(μ-ONep)$_2$(ONep)(HONep)$_3$(py)]$_2$ (**3**).[1] This species adopted a unique structural type in comparison to the six other $Ba(OR)_2$ species previously crystallographically characterized.[37,41−46] Since that time, only one additional '$Ba(OR)_2$' has been added to the literature, (OPP)Ba(μ-OPP)$_3$Ba.[34] Because **3**[1] was never fully disclosed in terms of synthesis or structure, the experimental details and information about this derivative have been included in this manuscript.

As mentioned, we are interested in producing $A^ETi(OR)_6$ precursors to systematically generate A^ETiO_3 nanoparticles. A search of the literature reveals numerous $A^ETi(OR)_6$

(35) Evans, W. J.; McClelland, W. G.; Greci, M. A.; Ziller, J. W. *Eur. J. Solid State. Inorg. Chem.* **1996**, *33*, 145−156.
(36) Dunne, J. P.; Tacke, M.; Selinka, C.; Stalke, D. *Eur. J. Inorg. Chem.* **2003**, 1416−1425.
(37) Tesh, K. F.; Hanusa, T. P. *Chem. Commun.* **1991**, 879−881.
(38) Hitchcock, P. B.; Lappert, M. F.; Lawless, G. A.; Royo, B. *Chem. Commun.* **1990**, 1141−1142.
(39) Drake, S. R.; Streib, W. E.; Chisholm, M. H.; Caulton, K. G. *Inorg. Chem.* **1990**, *29*, 2707−2708.
(40) Drake, S. R.; Otway, D. J.; Hursthouse, M. B.; Malik, K. M. A. *Polyhedron* **1992**, *11*, 1995−2007.
(41) Caulton, K. G.; Chisholm, M. H.; Drake, S. R.; Folting, K. *Chem. Commun.* **1990**, 1349−1351.
(42) Caulton, K. G.; Chisholm, M. H.; Drake, S. R.; Folting, K.; Huffman, J. C.; Streib, W. E. *Inorg. Chem.* **1993**, *32*, 1970−1976.
(43) Borup, B.; Samuels, J. A.; Streib, W. E.; Caulton, K. G. *Inorg. Chem.* **1994**, *33*, 994−996.
(44) Tesh, K. F.; Hanusa, T. P.; Huffman, J. C.; Huffman, C. J. *Inorg. Chem.* **1992**, *31*, 5572−5579.
(45) Miele, P.; Foulon, J.-D.; Hovnanian, N. *Polyhedron* **1993**, *12*, 209−219.
(46) Drake, S. R.; Streib, W. E.; Folting, K.; Chisholm, M. H.; Caulton, K. G. *Inorg. Chem.* **1992**, *31*, 3205−3210.

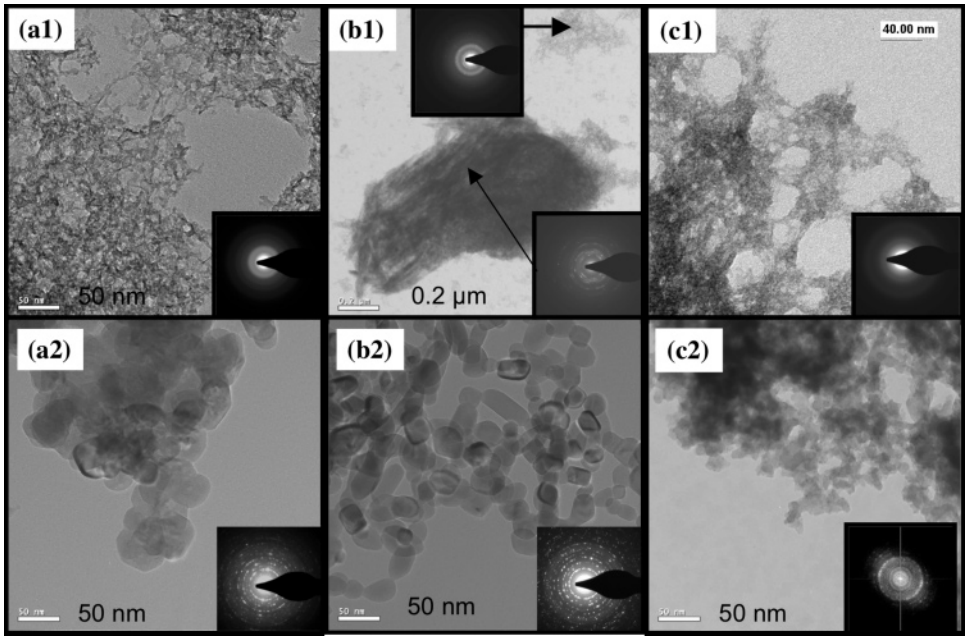

Figure 7. TEM images of nanoparticles from the MeIm/H_2O route and the respective stoichiometric mixtures of the individual precursors and [Ti(μ-ONep)(ONep)$_3$]$_2$: for the as-prepared particles from (a1) **1**, (b1) **2**, and (c1) **3**, and images of the calcined (650 °C) nanoceramics from (a2) **1**, (b2) **2**, and (c2) **3**.

species[15−17,19−24,47] with a variety of A^E:Ti ratios, but most are predominately Ti-rich, adopting a variety of cluster types. Possession of the same structure of the precursor is of interest for minimizing processing variations and allow for a systematic investigation of cation effects on the final material. One set of isostructural $A^ETi(OR)_6$ compounds has been identified as $A^E[(\mu_3\text{-}OR)_2(\mu\text{-}OR)_3Ti_2(OEt)_4]_2$ (A^E = Ca,[16,18] Sr,[20] Ba[16,18]); however, the ratio of A^E:Ti is 1:4, which we felt was too rich in Ti to be useful as a single-source precursor for A^ETiO_3 nanoparticle production.

Neopentoxide derivatives have found utility in the production of materials because of their high solubility, high volatility, low temperature, and clean decomposition pathways. It was reasoned that the increased steric bulk of the ONep ligand versus that of the OEt would reduce the A^E:Ti ratio. Therefore, we initiated our investigation by mixing stoichiometric amounts of the A^E and Ti(ONep)$_4$ derivatives. In an attempt to identify the active species in these reactions, we isolated the products by crystallization. Details of the synthesis and characterization of these precursors and the subsequent nanoparticles formed by solution and solvothermal routes are discussed below.

Precursor Synthesis. Because the ONep derivatives of Sr (**2**) and Ba (**3**) were available[1,26] (see Figure 1), we initiated our studies with these precursors. The synthesis of these compounds involves the reaction of the bulk metal with H-ONep (eq 1) in THF at elevated temperatures for extended periods of time. After being dried and redissolved, crystals were isolated from py. The Sr precursor (**2**) has been previously described[26] to adopt a complex cluster of five Sr atoms surrounding a hypervalent oxygen atom in a square base pyramidal geometry with a variety of bridging and terminal ONep ligands, Figure 1a.

$$A^{E\circ} + (\text{xs})\ \text{H-ONep} \xrightarrow[\Delta]{\text{solvent}} \text{“}A^E(\text{ONep})_2(\text{solv})\text{”} \qquad (1)$$

$$A^E = \text{Sr, Ba; solvent} = \text{THF, py}$$

Although a brief description of **3** was previously discussed,[1] the structural aspects were not fully disseminated. The Ba derivative adopts a standard M_4O_{14} geometry using a variety of μ_3-ONep, μ-ONep, and terminal ONep, H-ONep, or py ligands to complete the octahedral (Oh) geometry around each metal center. A structural plot of **3** is shown in Figure 1c, and details for collection parameters are shown in Table 1. This structure type is unique among the literature-reported Ba(OR)$_2$, which adopt cubic, complex clusters or solvated monomers and dinuclear species.[34,37,41−46] Of this family, **3** most resembles the tetramethylethylenediamine (TMEDA) phenoxide (OPh) derivative [Ba$_3$(μ_3-OPh)$_3$(μ-Ph)$_3$-(TMEDA)$_2$]$_2$.[41] The bond distances and angles of **3** are consistent with the OPh derivative and the other derivatives.[34,37,41−46] In addition, isolation of the product used to generate **3** from THF instead of py led to an isostructural species identified as **A**, wherein several of the H-ONep solvent ligands were replaced with THF solvent molecules, Figure 1b.

Attempts to synthesize the Ca derivative (**1**) in a similar manner as noted for **2** and **3** using eq 1 were not successful. Therefore, it was necessary to synthesize it from an alternative approach. Due to our success with amide alcoholysis exchange to generate “Ca(OR)$_2$”,[12] we tried to synthesize **1** from eq 2. Unfortunately, we have not been able to isolate crystalline material from this process.

$$Ca(N(SiMe_3)_2)_2 + 2\ \text{H-ONep} \xrightarrow{\text{py}} \text{“}Ca(ONep)_2\text{”} \qquad (2)$$

Alkaline Earth Titanium Derivatives. Our initial attempts to synthesize $A^ETi(OR)_6$ derivatives focused on

(47) Yanovskaya, M. I.; Turevskaya, E. P.; Yanovskaya, M. I.; Kessler, V. G.; Turova, N. Y.; Pisarevskii, A. P.; Struchkov, Y. T. *Zh. Neorg. Khim. (Russ.)* **1995**, *40*, 355.

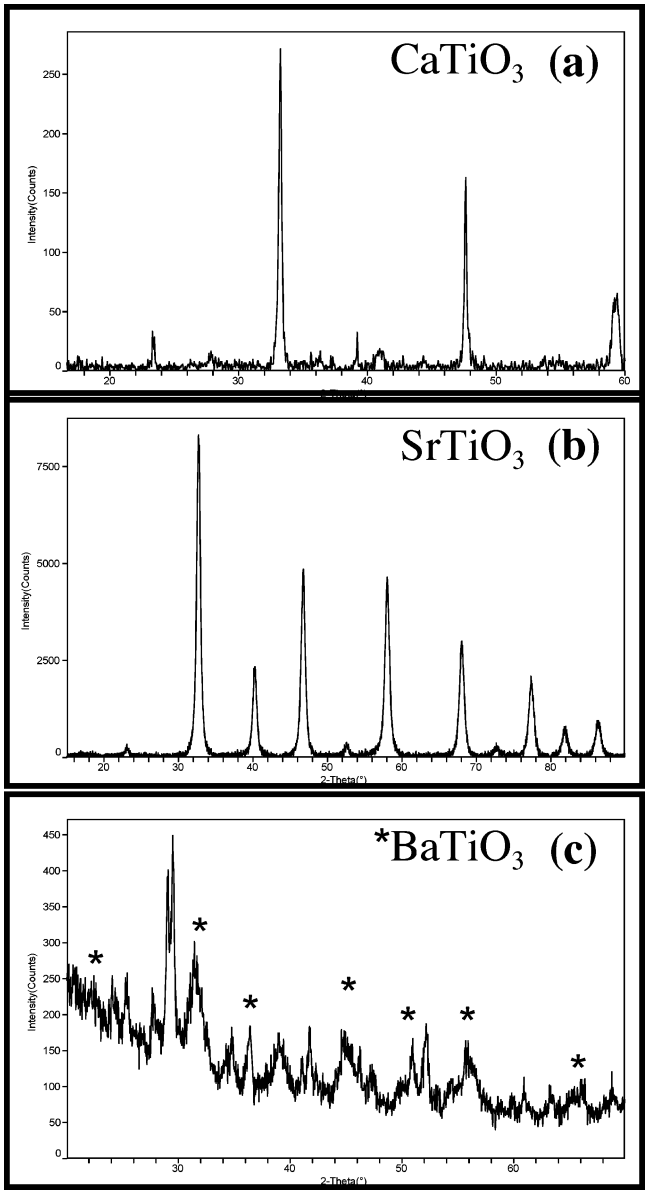

Figure 8. XRD patterns of calcined (650 °C) nanoceramics from the MeIm/H_2O route and the respective stoichiometric mixtures of the individual precursors and $[Ti(\mu\text{-ONep})(ONep)_3]_2$: (a) **1** made $CaTiO_3$, (b) **2** made $SrTiO_3$, and (c) **3** made $BaTiO_3$ and Ba_2TiO_4.

generating a stoichiometric 1:1 mixture of both cations. Therefore, **1**−**3** were dissolved in py and a stoichiometric amount of $[Ti(\mu\text{-ONep})(ONep)_3]_2$ was added. For **2** and **3**, the reaction mixture remained clear. For **1**, a precipitate immediately formed upon the addition of H-ONep to the amide; therefore, an in situ process in which H-ONep was added to a solution of $Ca(N(SiMe_3)_2)_2$ mixed with $[Ti(\mu\text{-ONep})(ONep)_3]_2$ was used. For all three reactions, X-ray quality crystals were isolated by the evaporation of the volatile component of each of these reactions. Due to the differences in the structures of **2** and **3**, it was surprising that product from all three reactions yielded compounds of general formula $A^E[Ti(ONep)_5(py)]_2$ (A^E = Ca (**1a**), Sr (**2a**), Ba (**3a**)). A representative structure of this species is shown in Figure 2. All attempts to isolate 1:1 species were unsuccessful; therefore, we optimized the synthesis to a 1:2 reaction ratio (eq 3).

$$[Ti(\mu\text{-ONep})(ONep)_3]_2 + \text{“}A^E(ONep)_2\text{”} \xrightarrow{py} (py)A^E[Ti(ONep)_5]_2 \quad (3)$$

$$A^E = Ca, Sr, Ba$$

The bulk materials of **1a**−**3a** were characterized by a variety of analytical methods. FT−IR data revealed the disruption of **2** and **3** had occurred and ONep, μ-ONep ligand, and coordinated py were present. Further, the spectra of **1a**−**3a** were nearly identical, indicating that these products had similar constructs. Elemental analyses were consistently low in the amount of detected carbon for each sample. This variation was attributed to the volatility of the coordinated H-ONep or py, which is often noted for these types of compounds.[25,48] Single-crystal X-ray diffraction studies were undertaken to further assist in identifying the compounds.

The single-crystal X-ray structures of **1a**−**3a** are unique among the previously isolated $A^ETi(OR)_6$ species.[15−17,19−24,47] Details for the collection parameters are shown in Table 1. For **1a**−**3a**, the A^E cation adopts an octahedral coordination using two py, and two sets of μ-ONep ligands that each bind to Ti. Both Ti metal centers adopt a square pyramidal geometery using the above μ-ONep ligands and terminal ONep ligands. The introduction of the sterically hindering ONep ligand was successful in reducing the stoichiometry of the A^E:Ti ratio to 1:2, which we thought may be acceptable for nanoparticle synthesis due to the reported volatility of “$Ti(ONep)_4$” moieties.[25,48] It should be noted that the thermal ellipsoids for **1a**−**3a** are slightly enlarged because of disorder associated with the terminal ligands. To improve the stability of this refinement, restraints were applied to the ONep ligands, which caused an elevated residual error, but did not change the established connectivity.

Solution Behavior. Because **1a**−**3a** were to be used in a solution synthesis of nanoparticles, it was of interest to determine whether the structure remained intact or not in solution. For each sample, crystalline material was redissolved in py-d_5, and ^1H and $^{13}C\{^1H\}$ NMR spectra were obtained. The ^1H and ^{13}C NMR revealed only one set of ONep peaks ($OCH_2C(CH_3)_3$) for **1a**−**3a** and **3**, indicating that both the terminal and bridging ONep ligands were rapidly exchanging in solution at room temperature. Low-temperature NMR data were prevented from being collected because of the rapid precipitation of the sample as the temperature decreased.

Nanoparticle Synthesis. The syntheses of complex A^E-TiO_3 nanoparticles using **1a**−**3a** followed two routes: (a) solution precipitation and (b) solvothermal. The first was a solution route that we have used extensively in our laboratory for the production of high-quality nanomaterials, such as $Co(OH)_2$,[49] ZnO,[12] and CaO.[12,13] The process involves the introduction of a metal alkoxide into a refluxing solution of the strong Lewis base 1-methylimidazole and water (MeIm/H_2O = 14.5/0.5 mL), which acts as an oxidant. Alternatively,

(48) Gallegos, J. J.; Ward, T. L.; Boyle, T. J.; Rodriguez, M. A.; Francisco, L. P. *Chem. Vapor Deposition* **2000**, *6*, 21−26.
(49) Boyle, T. J.; Rodriguez, M. A.; Ingersoll, D.; Headley, T. J.; Bunge, S. D.; Pedrotty, D. M.; De'Angeli, S. M.; Vick, S. C.; Fan, H. *Chem. Mater.* **2003**, *15*, 3903−3912.

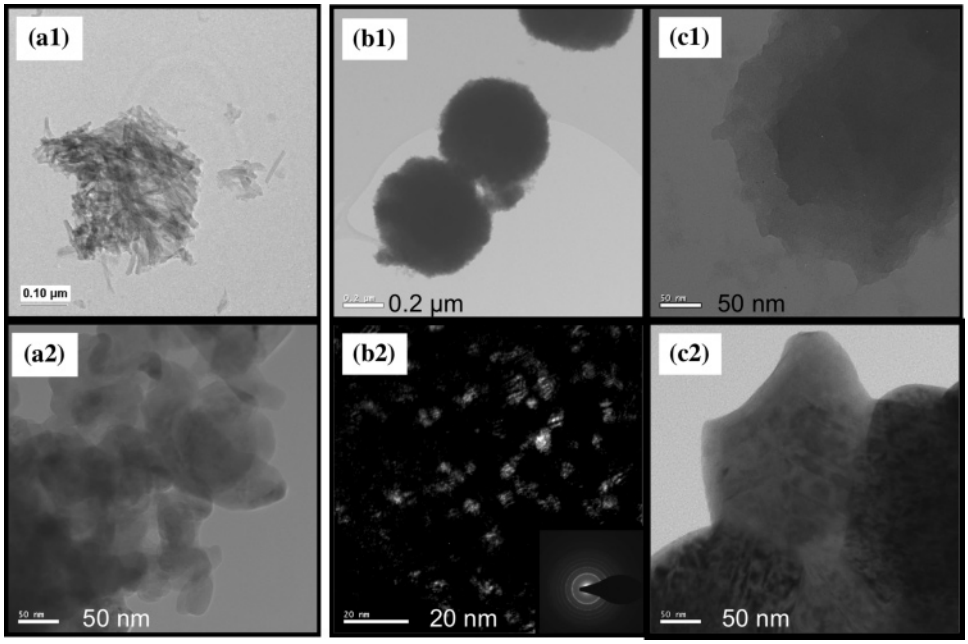

Figure 9. TEM images of nanoceramics from the solvothermal route and the respective single-source precursor: (a1) **1a** as-prepared, (a2) **1a** calcined (650 °C), (b1) **2a** as-prepared, (b1) DF of **2a** as-prepared, (c1) **3a** as-prepared, and (c2) **3a** calcined (650 °C).

a solvothermal route involving a Parr digestion bomb with BzOH has proven to be useful for the production of high-quality nanoparticles and was also explored.[8] Further, to determine the changes induced by the single-source precursors, we compared results to stoichiometric mixtures of the individual components (**1**, **2**, and **3**) with $[Ti(\mu\text{-ONep})(ONep)_3]_2$. A summary of the results for both methods is presented in Tables 2 and 3.

Solution Precipitation Route. The A^ETiO_3 precursor solutions were prepared by dissolving the desired precursors in py followed by injection into a MeIm/H_2O solution at reflux temperature and allowing it to react for 30 min. The results presented below are broken into two sections to simplify the discussion: single-source and stoichiometric mixtures.

Single-Source. Upon injection of the single-source precursor (**1a**−**3a**), dissolved in py into the refluxing MeIm/H_2O solution, a white precipitate immediately formed. TEM images for these particles were obtained and are shown in Figure 3. Energy dispersive spectroscopic (EDS) analyses confirmed the presence of (Ca,Ti), (Sr,Ti), and (Ba,Ti) for the **1a**−**3a** precipitates, respectively. For **1a** (Figure 3a1), amorphous agglomerated particles were isolated, whereas **2a** (Figure 3b1) possessed two distinct morphologies: polycrystalline nanorods and amorphous nanodots as determined by selected area electron diffraction (SAED). The crystallite sizes of the rods were too small to give useful powder diffraction patterns; therefore, the polycrystalline ring pattern was used to calculate *d*-spacings that were compared to SrO, TiO_2, and $SrTiO_3$. On the basis of these calculations, it was determined that a crystalline TiO_x species formed as an intermediate under the reaction conditions. The as-prepared particles generated from **3a** (Figure 3c) had an appearance similar to that of the particles formed from **1a** and were also found to be amorphous by SAED.

To convert these as-prepared particles to the perovskite phase, the isolated particles were rinsed with EtOH, air-dried, ground by mortar and pestle, and calcined at 650 °C under argon. TEM images of the calcined powders are shown in Figures 3a2−c2 for **1a**−**3a**, respectively. All three images show agglomerated particles on the order of 10−50 nm. Verification of the particle size distribution and morphology at the micrometer level was confirmed by SEM for **2a** (Figure 4) and revealed no rodlike morphologies, but particles <100 nm had formed during the crystallization process. The PXRD patterns for the calcined particles generated by **1a**−**3a** are shown in Figure 5. For **1a**, a mixed phase of TiO_2, CaO, and $CaTiO_3$ was detected (Figure 5a), whereas for **2a** (Figure 5b) and **3a** (Figure 5c), the cubic A^ETiO_3 pattern with a minor carbonate phase formed. The average crystallite size for the respective samples calculated from the (110) was determined to be ∼20 and ∼12 nm for $SrTiO_3$ and $BaTiO_3$, respectively, by the Scherrer equation.

Of the three perovskite powders, nanocrystalline $BaTiO_3$ can adopt a tetragonal symmetry that can not be determined by PXRD data alone. Smaller crystallites and the 1% difference between the *c*/*a* unit-cell parameters make it difficult to observe the characteristic separation of the (200) into (200) and (002) near $2\theta = 45°$ because of line broadening. To verify tetragonality, we collected a Raman spectrum (Figure 6) of the $BaTiO_3$ powder synthesized under these reaction conditions and $BaTiO_3$ formed in the subsequent reaction conditions described below. The spectrum, Figure 6a, shows vibrational modes associated with the tetragonal phase of $BaTiO_3$ with broad bands peaking near 304, 534, and 755 cm^{-1}.[50] The presence of CO_3^{-2} (1057 cm^{-1})[51] from the $BaCO_3$ phase was also observed for this calcined sample. A^ETiO_3 particles synthesized by a variety of soft chemistry methods contain residual carbonate when they are calcined at 650 °C. The full removal of the carbonate phase requires temperatures in excess of 900 °C.

(50) Perry, C. H. H., D. B. *Phys. Rev. Lett.* **1965**, *15*, 700−702.
(51) Frey, M. H. P., D. A. *Chem. Mater.* **1995**, *7*, 123−129.

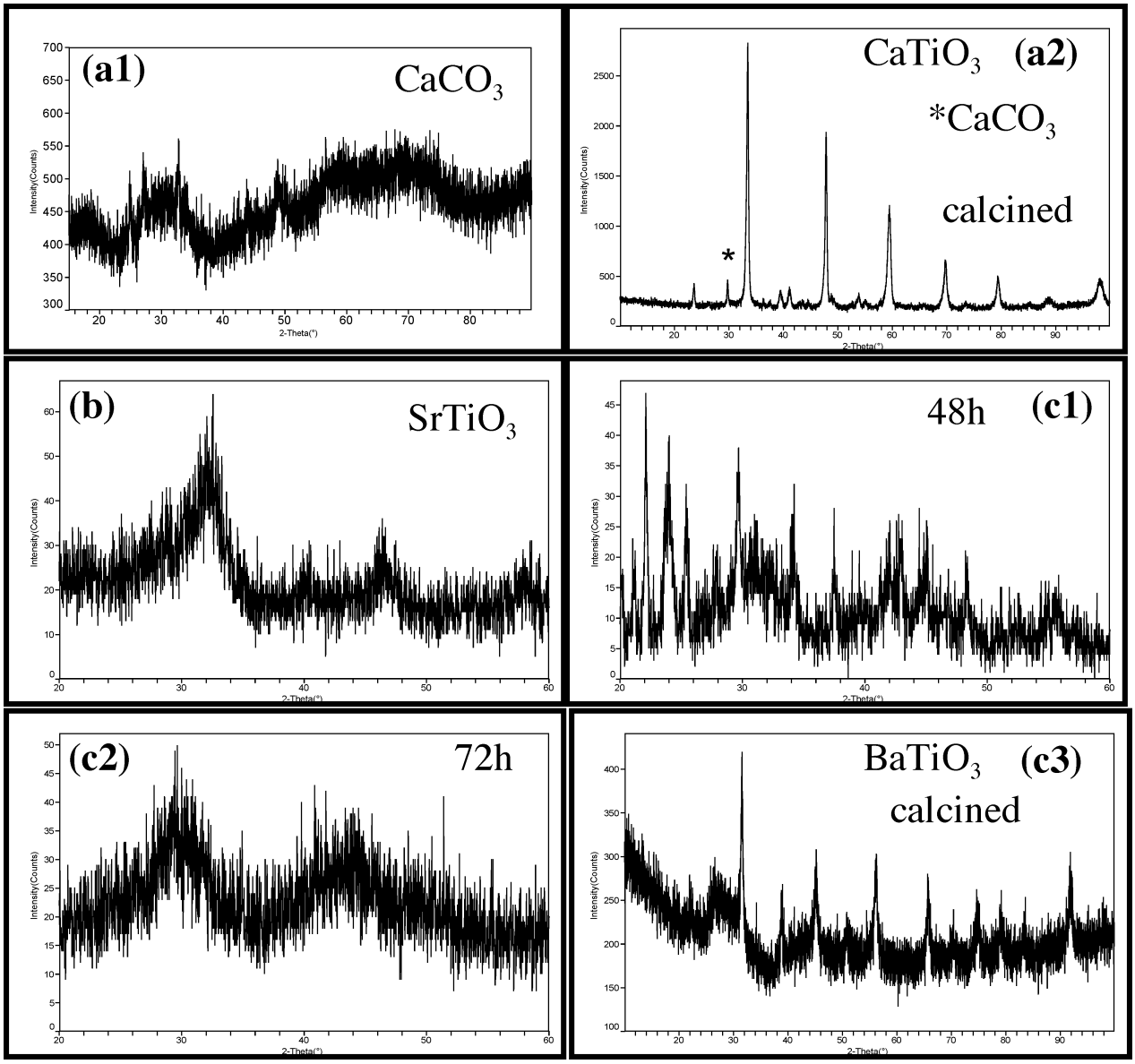

Figure 10. XRD patterns of nanoceramics from the solvothermal route and the respective single-source precursor: (a1) **1a** as-prepared made $CaTiO_3$ and $CaCO_3$; (a2) **1a** calcined (650 °C) made $CaTiO_3$ and $CaCO_3$; (b) **2a** as-prepared made $SrTiO_3$; (c1) **3a** as-prepared (48 h.) made TiO_2, $BaCO_3$, and $BaTiO_3$; (c2) **3a** as-prepared (72 h.); and (c3) **3a** calcined (650 °C) made $BaTiO_3$.

Stoichiometric Mixtures. To determine if the 1:2 A^E:Ti ratio of the single-source precursor had an effect on the crystallization and/or morphology of the oxides during the solution synthesis, stoichiometric solutions of **1**, **2**, and **3** with $[Ti(\mu\text{-ONep})(ONep)_3]_2$ were prepared and used as described for **1a**−**3a**. Again, each mixture formed a white precipitate upon injection and EDS confirmed the presence of (Ca,Ti), (Sr,Ti), and (Ba,Ti), respectively, with TEM and SAED images available in Figure 7. On the basis of electron microscopy results, it was determined that the A^E:Ti stoichiometry had no effect on the growth behavior during the MeIm/H_2O solution route. Similar morphological and crystalline characteristics were observed for these as-prepared particles when compared to the single-source precursors. The nanoparticles from **1** (Figure 7a1) and **3** (Figure 7c1) mixtures proved to be small amorphous nanoparticles; however, it is of note that the material isolated from **2** (Figure 7b1) again had a rodlike morphology and appeared to be polycrystalline TiO_x. These isolated particles were calcined under argon at 650 °C as noted for **1a**−**3a**.

The morphology of the calcined powders formed by the stoichiometeric mixtures are also shown in Figure 7. The spherical-like particles of **1** (Figure 7a2) are ∼50 nm in diameter and those of **3** (Figure 7c2) are ∼10 nm. Again, the particles are agglomerated as noted for the single-source species. For **2**, the rodlike morphology observed in the as-prepared sample was also no longer present and distinct ∼20−50 nm spherical and rectangular particles were formed under the same calcination conditions. In contrast to the single-source precursors, the PXRD patterns, Figure 8, show only oxide formation with different phases of the titanates. For the first system, the in situ synthesis of **1** in the solution of $[Ti(\mu\text{-ONep})(ONep)_3]_2$ led to the formation of orthorhombic $CaTiO_3$ nanoparticles with a calculated ∼23 nm crystallite size, Figure 8a. This is the room-temperature stable phase that will transform to the cubic phase at higher

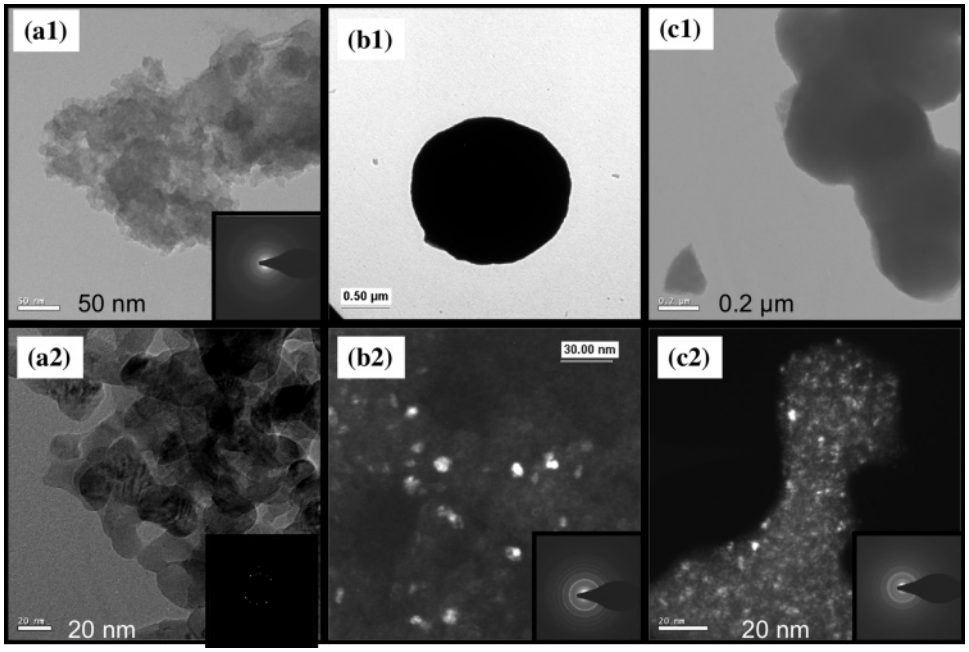

Figure 11. TEM images of nanoceramics from the solvothermal route and stoichiometric mixtures of the individual precursors and $[Ti(\mu\text{-ONep})(ONep)_3]_2$ for: (a1) **1** as-prepared, (a2) **1** calcined (650 °C), (b1) **2** as-prepared, (b1) DF of **2** as-prepared, (c1) **3** as-prepared, and (c2) DF of **3** as-prepared.

temperatures. For the reaction between **2** and $[Ti(\mu\text{-ONep})(ONep)_3]_2$, the nanoparticles were indexed to the cubic $SrTiO_3$ phase and had a calculated ~13 nm crystallite size, Figure 8b. The nanoparticles generated by the $BaTiO_3$ synthesis, however; were indexed to tetragonal $BaTiO_3$ and the metastable barium orthotitanate Ba_2TiO_4, Figure 8c. The Raman spectrum for this sample, Figure 6b, had broad characteristic tetragonal peaks (283, 544, and 720 cm^{-1}) and some residual carbonate not detected by PXRD (1061 cm^{-1}). The formation of the metastable Ba_2TiO_4 has been attributed to the decomposition of $BaCO_3$ and has also been observed in several sol−gel and chelate solution routes during the calcination process of green powders to the perovskites.[10]

Summary for the Solution Route. It appears that the MeIm/H_2O solution route immeditately hydrolyzes the alkoxides forming amorphous (Ca,Ti) and (Ba,Ti) nanomaterials but polycrystalline TiO_x rods and amorphous nanoparticles for (Sr,Ti). Under these conditions, the stoichiometry or the structure of the metal alkoxides did not influence the final morphology. It was necessary to further process the precipitates formed during the MeIm/H_2O route, and crystallization at elevated temperatures led to perovskite nanoparticles on the order of 10−15 nm. These results are in contrast to our early experiments with Zn alkyl alkoxides, which showed that crystalline ZnO readily formed under the same reaction conditions and may be due to the thermal energy needed to decompose the bimetallic alkoxides precursors.[13] It is interesting to note that the single-source precursors for **2a** and **3a** ($A^ETi(OR)_{10}$) produced the A^ETiO_3 pervoskite phase instead of $A^ETi_2O_5$. On the basis of Kirby's hypothesis[52] that the phase generated during the crystallization process of green powders is dictated by the single source A^E:Ti stoichiometry, one should expect our $A^ETi(OR)_{10}$ to produce $A^ETi_2O_5$ products. One reason for the synthesis of A^ETiO_3 versus $A^ETi_2O_5$ may be due to the volatility of excess "Ti-(ONep)$_4$" during the MeIm/H_2O nanoparticle reaction conditions. Overall, single-source precursors were found to not be necessary and to create more phases than the stoichiometeric mixtures.

Solvothermal. To generate crystalline nanoparticles without necessitating a calcination step, we chose to investigate a solvothermal route that utilized BzOH.[8] This method reportedly produced crystalline 10 nm perovskite particles from the in situ synthesis of Ba (or Sr) benzyl alkoxides and titanium isopropoxide ($Ti(OPr^i)_4$) to form a single-source precursor. Although a mechanism is proposed, no direct crystalline structural evidence of the bimetallic alkoxides synthesized from this procedure was provided. Therefore, we were interested in determining how our structurally characterized precursors would behave in this reaction system. Solutions were prepared by dissolving the desired precursor in BzOH to form clear pale yellow solutions. The individual solutions were transferred to the Teflon liner, sealed in the glove box, and then transferred out of the glove box to be heated in an oven at 200 °C for 48 h.

Single-Source Alkoxides. After being subjected to the described solvothermal conditions, the reactions typically yielded clear orange or yellow mother liquors that contained a milky white precipitate. The TEM and PXRD for these precipitates are shown in Figures 9 and 10. The morphology of the as prepared particles isolated from **1a** (Figure 9a1) were rods of 5 × 100 nm dimensions. The rods exhibited weak reflections that were indexed to vaterite (a metastable phase of $CaCO_3$) and orthorhombic $CaTiO_3$ (Figure 10a1). This powder was calcined in the furnace to help promote formation of phase-pure $CaTiO_3$ (~29 nm crystallite size) as identified by PXRD, Figure 10a2. A minor phase of $CaCO_3$ was also noted. After calcination, the rods were transformed into ~50 nm particles (Figure 9a2).

(52) Kirby, K. W. *Mater. Res. Bull.* **1988**, *23*, 881−890.

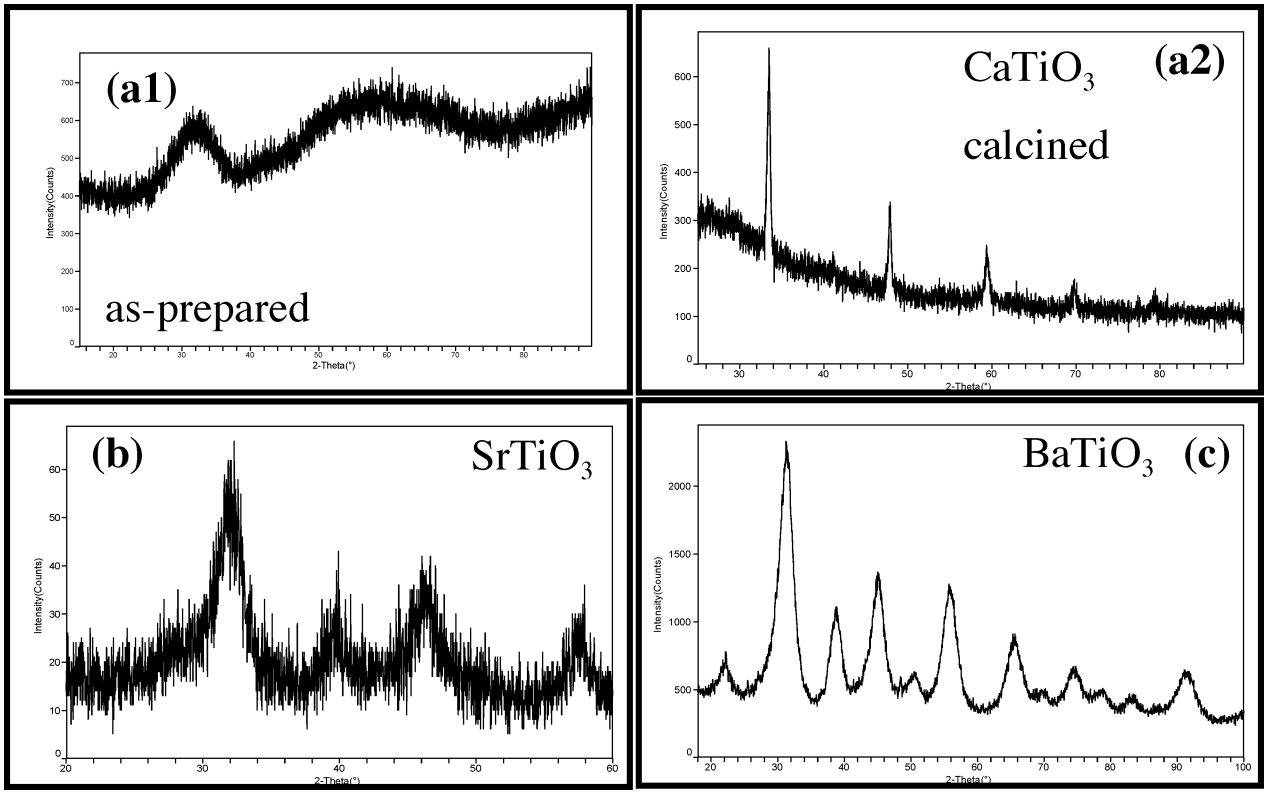

Figure 12. XRD patterns of nanoceramics from the solvothermal route and stoichiometric mixtures of the individual precursors and $[Ti(\mu\text{-ONep})(ONep)_3]_2$: (a1) **1** as-prepared, (a2) **1** calcined (650 °C) made $CaTiO_3$, (b) **2** as-prepared made $SrTiO_3$, and (c) **3** as-prepared made $BaTiO_3$.

For **2a**, the as prepared particles were indexed to phase pure cubic $SrTiO_3$ with a calculated size of ~6 nm, Figure 10b. The morphology of these particles (Figure 9b1) appears to be large spherical 0.5 μm particles; however, closer examination through dark-field (DF) imaging shows that these particles are really made up of 10 nm crystallites, Figure 9b2. The SAED ring pattern for these crystallites confirmed the PXRD results.

Analysis of the reaction products by PXRD for $BaTiO_3$ system from **3a** revealed a mixture of $BaCO_3$ and TiO_2 (Figure 10c1); however, by extending the solvothermal heating time from 48 to 72 h, the onset formation of a single phase occurred (Figure 10c2). Although the crystalline phase could not be identified by diffraction methods, Raman (Figure 6c) spectroscopy identified that the precipitate contained a mixture of TiO_x species and aromatic groups. The spectrum was dominated by intense bands from residual BzOH, whereas lower-intenstity bands peaking near 683, 840, and 889 cm^{-1} are similar to those found for species such as $Ti_2O_5^{-2}$, $Ti_3O_7^{-2}$, or $Ti_4O_9^{-2}$. The morphology for these as prepared particles (Figure 9c1) were 0.5 μm spheres. This sample was calcined at 650 °C under argon to facilitate crystal growth. The calcined particles were found to be ~100 nm (Figure 9c2) with observable ferroelectric domains. PXRD (Figure 10c3) also detected the tetragonal phase of $BaTiO_3$ with an average crystallite size calculated at ~30 nm.

Stoichiometric Mixtures. Because the solution results yielded nearly identical morphologies for the single-source and stoichiometric mixtures, it was of interest to determine how the stoichiometric mixtures would affect the final A^E-TiO_3 materials using solvothermal synthesis. TEM and PXRD results for these nanomaterials are shown in Figures 11 and 12. In contrast to the formation of rods produced by **1a**, stoichiometric reactions of **1** and $[Ti(\mu\text{-ONep})(ONep)_3]_2$ produced agglomerated particles, Figure 11a1. The phase of these particles could not be established by diffraction studies (Figures 11a1 and 12a1). After calcination of these particles, ~50 nm orthorhombic $CaTiO_3$ particles were produced that contained a residual amount of $CaCO_3$ (Figures 11a2 and 12a2). The average crystallite size calculated from Figure 12a2 was ~24 nm.

The formation of cubic $SrTiO_3$ and tetragonal $BaTiO_3$ from the reaction mixture of $[Ti(\mu\text{-ONep})(ONep)_3]_2$ with **2** and **3**, respectively, resulted in ~1 μm spherical particles that were similar to those observed from **2a** under solvothermal conditions. These ~1 μm spheres (images b1 and c1 of Figure 11) also contain nanometer-sized crystallites on the order of ~15 nm $SrTiO_3$ and 5−10 nm $BaTiO_3$, as observed by the dark-field TEM images (images b2 and c2 of Figure 11), respectively. The crystalline phases formed from **2** and **3** were determined (panels b and c of Figure 12) to be the cubic $SrTiO_3$ and tetragonal $BaTiO_3$ phases with a calculated average crystallite size of ~10 nm. Because of the intense fluorescence scatter, the Raman spectrum for $BaTiO_3$ was not obtained. This result may be due to surface chemistry or residual decomposition products around the nanoparticles.

Summary for the Solvothermal Route. Unlike the solution precipitation route, the solvothermal route allows for the autogenous pressure to be altered through solvent selection and temperature to promote crystallization during synthesis. Through the solovthermal method, crystalline A^ETiO_3 nanomaterials were directly synthesized on the baiss of a selection of precursor used. Unlike the synthesis of $CaTiO_3$

and $BaTiO_3$ from the single-source precursors (**1a** and **3a**), pure crystalline $SrTiO_3$ nanoparticles were synthesized without having to undergo further calcination procedures. For $SrTiO_3$, the stoichiometeric mixtures also directly produced a single perovskite phase, whereas the synthesis of pure $BaTiO_3$ was achieved only from the stoichiometric mixtures of **3** and $[Ti(\mu\text{-ONep})(ONep)_3]_2$. For our system, the as-prepared particles formed during the solvothermal synthesis appeared to be micrometer-sized spheres or rods that comprise nanometer-sized crystallites. We are exploring why rodlike materials were synthesized during the solvothermal and solution precipitation routes. The rodlike morphology observed for the solvothermal treatment of **1a** was lost during subsequent crystallization to achieve a phase pure $CaTiO_3$. This observation is similar to the transformation of the rods to particles, produced by the solution routes, involving **2a** and **2**. Thus far, PXRD and TEM analysis indicates that these rods are intermediates or metastable phases (i.e., TiO_x, $CaCO_3$).

Conclusion

We have synthesized and characterized an isostructural set of alkaline earth *neo*-pentoxide single-source precursors of identical structural arrangements (**1a**−**3a**). These precursors, coupled with a stoichiometric mixture of alkaline earth *neo*-pentoxide (**1**−**3**) precursors mixed with $[Ti(\mu\text{-ONep})(ONep)_3]_2$, were used in a solution precipitation or solvothermal route to generate A^ETiO_3 nanoparticles. Tables 2 and 3 outline the various results from this mixture of precursors and processes. Comparison of single-source and stoichiometric mixtures point to the stoichiometeric precursors as the better choice to generating single-phase A^ETiO_3 from the MeIm/H_2O route; however, sets of precursors required calcinations to achieve full crystallization. Through solovothermal synthesis routes, single-source and stoichiometric mixtures both gave favorable crystalline results for Sr and Ba. Interestingly, there appears to be a significant cation effect that determines the final crystalline phase: Ca samples generated carbonates and perovskites; Ba formed carbonates, orthotitanates, and pervoskites; Sr formed pure perovskites with a very small residual amount of carbonate.

Although this study indicates that the single-source precursors were not necessary to produce A^ETiO_3 nanoparticle, isolation of the single crystals from the stoichiometeric mixtures of A^E and Ti gives insight to how the ONep derivatives behave in solution. Therefore, it is not unreasonable that **1a**−**3a** are active components of the stoichiometric mixtures; however, more work to understand how the solvents effect the structures of these compounds is necessary to unequivocally establish the active components. The electronic properties of the phase-pure nanomaterials produced by these synthetic methods are currently being evaluated and these results will be reported later.

Acknowledgment. The authors thank the Office of Basic Energy Sciences of the Department of Energy for its support of this work. Sandia is a multiprogram laboratory operated by Sandia Corporation, a Lockheed Martin Company, for the U.S. Department of Energy's National Nuclear Security Administration under Contract DE-AC04-94AL85000.

CM061798+